(Received 30 May 2024, Accepted 8 July 2024, Scheduled 11 July 2024)

A Hybrid Excitation Variable-Leakage-Flux Machine with Magnetic-Bridge for Electric Vehicle

Ruipan Lu, Xinlong Huang, Zhangqi Liu*, and Xiping Liu

School of Electrical Engineering and Automation, Jiangxi University of Science and Technology, Ganzhou 341000, Jiangxi, China

ABSTRACT: A hybrid excitation variable-leakage-flux machine (HE-VLFM) for electric vehicles is presented in this paper, which places the excitation windings on the outer side of the stator and provides an axial magnetic field through the magnetic-conducting ring and magnetic-conducting bridge. The HE-VLFM proposed in this paper has a rotor permanent magnet to provide the main magnetic field and an excitation winding to provide a variable auxiliary magnetic field, which can fulfill the requirements of the electric vehicle drive system with large torque at low-speed and wide speed regulation range. The electromagnetic performance of the proposed HE-VLFM is evaluated using the equivalent magnetic circuit method and three-dimensional finite element analysis, and the results show that the HE-VLFM has a well-developed regulating flux capability.

1. INTRODUCTION

Interior permanent magnet synchronous machine (IPMSM) has received widespread attention for its remarkable advantages such as high power density, high integration, high overload capability, and flexible driving [1–3]. In electric vehicles, aerospace, vessels, domestic appliances, and other application areas, higher requirements have been placed on the performance indexes of permanent magnet machines such as volume, weight, and reliability [4–6]. However, the working point of a conventional permanent magnet machine is basically fixed, and the air gap field is difficult to adjust. It increases the capacity of the inverter and causes the machine to be less efficient at high speed [5–8]. Meanwhile, because the negative d-axis current i_d produces armature reacting with the flux of opposite polarity to that of the permanent magnet, there is a risk of irreversible demagnetization of the permanent magnet [9, 10].

Variable-leakage-flux permanent magnet machines have the advantages of wide constant-power speed range and lower flux-weakening current at high-speed operating condition, thus there is competitiveness in their application as drive machines in electric vehicles [11–13]. However, it was found that the leakage bypass in variable leakage-flux machines reduces the output torque somewhat and affects the load carrying capacity of the machine.

Hybrid excitation permanent magnet machines (HEPMMs) have become an alternative solution for these industrial applications by using separate excitation windings to regulate air-gap flux. At low-speed operating condition, the peak torque in the starting region is increased by a positive DC excitation current. At high-speed operating condition, the negative DC excitation current weakens the magnetic field and widens the speed range [14–19]. A variety of structures and topologies for HEPMMs have been proposed, and their principles and performance have been extensively studied in the literature. According to the distribution of field winding, it can be divided into rotor field winding type HEPMM and stator field winding type HEPMM. In [20], a surface-mounted dual excitation synchronous machine is designed to obtain a wide range of speed, and the total losses can be reduced over the wide range of speed operation. A hybrid excitation interior permanent magnet synchronous machine is investigated in [21] to address the low efficiency of conventional electrically excited machines up to several megawatts in the low power region. However, the above machines require the introduction of slip rings and brushes, which reduces the reliability of the machines and limits further increases in speed and power density. Stator field winding type HEPMMs can be viewed as evolving from the introduction of an excitation winding topology in conventional permanent magnet synchronous machines, which can be brushless. A hybrid excitation synchronous machine with magnetic shunting rotor is developed in [22] for the electromagnetic performance and mechanical strength of the machine. A single/double-ended excitation winding structure is proposed, and the field distribution, back-electromotive force (EMF), flux regulation performances, and torque characteristics of the machine under different excitation currents are investigated. The results show that the flux linkage regulation capability can be improved by more than three times. A hybrid excitation brushless DC generator consisting of structure-parallel permanent magnet machine part and flux modulation machine part is proposed in [23]. The bidirectional flux regulation capability of the machine enables flux regulation over a wide range. In [24], a hybrid excitation synchronous machine with consequent pole is proposed for a wide regulation range of the machine. The permanent magnet magnetic circuit and electric excitation magnetic circuit are in parallel relationship. Based on the current density and the minimum size of the machine, the inner and outer stator diameters

* Corresponding author: Zhangqi Liu (liuzhq@jxust.edu.cn).

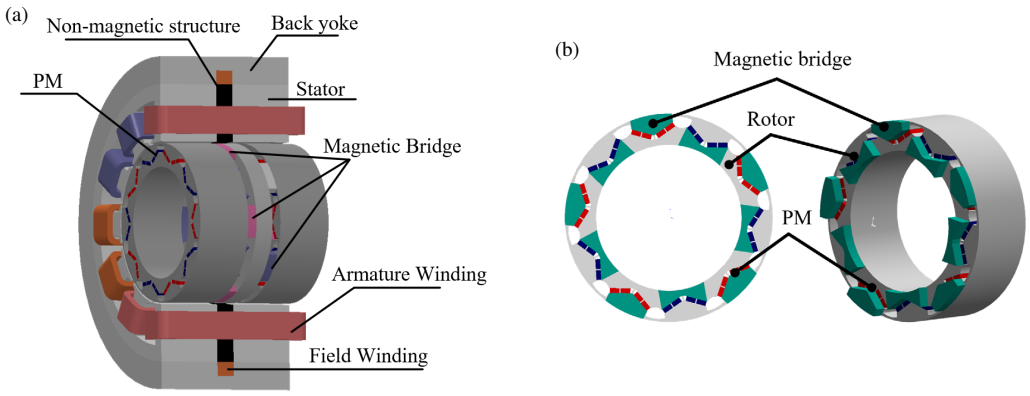

FIGURE 1. Proposed HE-VLFM.

and the excitation magnetic potential are optimized to achieve the weakening and strengthening of the magnetic field.

In this paper, a constant speed machine with stator and rotor divided into three parts and V-shaped rotor based on magnetic conducting bridge is proposed. The inner and outer magnetic bridges connecting the two sides of the rotor and stator cores are designed to provide an axial magnetic circuit in which the excitation winding can be operated without brushes or slip rings. The design and its operating principle are presented and verified by equivalent magnetic circuit (MEC) method and 3D finite element analysis, and the results show that the design has good flux regulation capability under both flux-enhancing and flux-weakening operating conditions.

2. STRUCTURE AND PRINCIPLE

2.1. Machine Topology

The topological structure of the proposed HE-VLFM with 12-slot/10-pole configuration is illustrated in Fig. 1. HE-VLFM is composed of stator, rotor, permanent magnet, armature winding excitation winding, back yoke, magnetic bridge, and non-magnetic structure. In order to enhance the flux-weakening capability of the HE-VLFM, it is intentionally provided with a wide leakage bypass between neighboring V-type permanent magnets. The stator side is centrally wound with double layers of fractional slot centralized winding, and the PMs are divided into two segments. Correspondingly, the internal flux barrier is constructed in the q-axis magnetic circuit on the rotor side to reduce the q-axis inductance. In addition to this, the flux barrier is also provided at the end of the PMs, whose main purpose is to allow the leakage flux in the flux bridge to form a crosslink with the q-axis armature flux so that the leakage-flux can be more easily controlled by the q-axis armature magnetic potential, further increasing the flux-weakening capability of the machine.

The stator core is divided into three parts, whose two sides are made of silicon steel, and the middle part is made of non-magnetic aluminum oxide material. An external magnetic bridge connects the two sides of the stator core to form an axial external magnetic flux path. The rotor core is also divided into three segments at the same location, where the two sides are of conventional spoke rotor structure, and the middle part is an internal magnetic bridge connecting the two sides of the rotor core to form an axial internal magnetic flux path. The field windings are embedded inside the back yoke through the stator-side non-magnetic alumina material, which provides a simple spatial layout compared to most HEPMMs. The basic geometric parameters of the proposed HE-VLFM are listed in Table 1.

TABLE 1. Basic design specifications of HE-VLFM.

Parameter	Unit	Value
Out radius of stator	mm	150
Out radius of rotor	mm	89.4
Stack length of the machine	mm	80
Rated voltage	V	220
Rated current	A	14
Rated speed	r/min	1500
Pole slot fitting	–	10/12
Number of turns	–	15
Air-gap length	mm	0.7
Rated power	Kw	2.5
Current density	A/mm^2	5
Length of magnetic bridge	mm	5
Length of magnet	mm	3

2.2. Operating Principle

The working principle of the proposed HE-VLFM is shown in Fig. 2, where Fig. 2(a) depicts the magnetic circuit of the machine under excitation flux path and permanent magnet flux path. The main magnetic flux generated by the PMs forms a closed magnetic circuit through the permanent magnets, air gap, rotor core, and stator core. The HE-VLFM different magnitudes of output torque depending on the load and the q-axis current play a decisive role in the output torque of the machine. As the machine is under light load condition, the q-axis current is small; the q-axis armature flux is small; and the saturation of the machine is shallow. When the field winding is excited by an field winding (FW) current, the FW flux passes through the magnetic bridge, stator core, air gap, rotor core, and back yoke

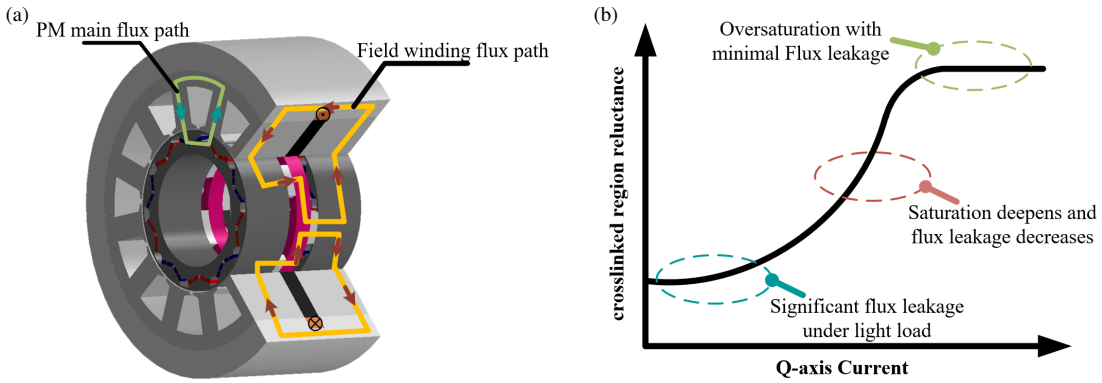

FIGURE 2. Operating principle of HE-VLFM. (a) Magnetic circuit of HE-VLFM under FW flux path and PM flux path. (b) Variable leakage flux principle.

as shown by the yellow line in Fig. 2(a). Depending on the direction of the excitation magnetic circuit, the excitation current passing in different directions can realize the enhancement or weakening of the flux. Specifically, the polarity of the excitation flux under neighboring poles is reversed and alternately staggered in the axial position of the machine. Therefore, it can effectively regulate the flux and direction of the flux, and thus the main flux can be well controlled.

A dynamic mathematical model based on the *dq*-axis synchronized rotating coordinate system was developed. The flux linkage equation can be expressed as:

$$\lambda_d = L_d i_d + M_{sf} i_f + \lambda_{pm} \tag{1}$$

$$\lambda_q = L_q i_q \tag{2}$$

$$\lambda_f = \frac{3}{2} M_{sf} i_f + L_f i_f + \lambda_{mf} \tag{3}$$

where λ_d, λ_q, λ_f, λ_{pm}, and λ_{mf} are the d-axis and q-axis flux linkages, field winding total flux linkage, PM flux linkage, and field winding flux linkage coupled with PM, respectively. L_d is the d-axis inductance, L_q the q-axis inductance, L_f the self-inductance of field winding, and M_{sf} the peak value of mutual-inductance of armature winding and excitation winding. i_d is the d-axis current, i_q the q-axis current, and i_f the FW current.

The voltage equations are expressed as:

$$u_d = R_s i_d + \frac{d\lambda_d}{dt} - w_e \lambda_q \tag{4}$$

$$u_q = R_s i_q + \frac{d\lambda_q}{dt} - w_e \psi_d \tag{5}$$

$$u_f = R_f i_f + \frac{d\lambda_f}{dt} \tag{6}$$

where u_d, u_q, u_f are the d-axis and q-axis voltages, field winding voltage, respectively; R_s, R_f are the armature winding reluctance and field winding reluctance, respectively; w_e is the electrical angular frequency.

The electromagnetic torque equations are expressed as:

$$T_{pm} = \frac{3}{2} P_r i_q \lambda_{pm} \tag{7}$$

$$T_r = \frac{3}{2} P_r i_d i_q (L_d - L_q) \tag{8}$$

$$T_f = \frac{3}{2} P_r M_{sf} i_f i_q \tag{9}$$

$$T_e = T_{pm} + T_r + T_f \tag{10}$$

where P_r is the number of rotor pairs, T_e the total electromagnetic torque, T_{pm} the PM torque generated by the interaction between the PM flux linkage and armature current, T_r the reluctance torque generated by the variable of armature winding self-inductance and mutual inductance due to the variable of the rotor position, and T_f the additional torque compared to PMSM.

Since the magnetic permeability of the leakage bypass and magnetic bridge is large, much larger than that of the air gap, the magnetic flux generated by the permanent magnets will form a loop through the leakage bypass and magnetic bridge, thus generating a large amount of leakage flux inside the rotor. As the load increases, the flux generated by the q-axis current gradually increases, and the degree of saturation in the crosslinked region increases due to the superposition of the q-axis current flux, which makes the reluctance of the region larger, and therefore the leakage is reduced accordingly. The variation curve of the reluctance of the crosslinked region with the q-axis current is shown in Fig. 2(b).

At sufficiently large loads, the machine is in a state of oversaturation, and the reluctance in the crosslinked region is at its maximum, at which point the HE-VLFM has the least amount of flux leakage. As a result, the leakage flux of the HE-VLFM can be automatically adjusted as the load changes. In order to fully utilize the core material, the machine is rated to operate in saturation. In addition, the magnetic saturation effect of the machine cannot be neglected, and the traditional d-axis flux linkage and torque calculation formula for permanent magnet machines is no longer applicable. The new calculation formula is as follows:

$$\Phi_d = \begin{cases} \Phi_{pm0} + k i_q + L_d(i_d, i_q) i_d, & (i_q < i_{qr}) \\ \Phi_{dm} + L_d(i_d, i_q) i_d, & (i_q \geqslant i_{qr}) \end{cases} \tag{11}$$

$$k = \frac{\Phi_{dm} - \Phi_{pm0}}{i_{qr}} \tag{12}$$

$$T = \begin{cases} \frac{3}{2} P \left\{ \Phi_{pm0} i_q + k i_q^2 + [L_d(i_d, i_q) - L_d(i_d, i_q)] \, i_d i_q \right\}, \\ (i_q < i_{qr}) \\ \frac{3}{2} P \left\{ \Phi_{dm} i_q + (L_{dm} - L_{qm}) \, i_d i_q \right\}, \\ (i_q \geqslant i_{qr}) \end{cases} \tag{13}$$

where Φ_{pm0} is the no load PM flux linkage, k the scale factor, P the number of poles, L_d the d-axis inductance, L_q the q-axis inductance, i_d the d-axis current, i_q the q-axis current, i_{qr} the q-axis at oversaturation, and Φ_{dm} the d-axis flux linkage at oversaturation.

3. MAGNETIC EQUIVALENT CIRCUIT

In order to determine the main factors affecting the strength of the magnetic field of the main air gap flux, the equivalent magnetic circuit model of the machine is established based on the structural characteristics and magnetic circuit of the machine.

The three-dimensional equivalent magnetic circuit of HE-VLFM is illustrated in Fig. 3(a), where F_{pm} is the PM magnetomotive force (MMF); F_{fw} is the field winding MMF, R_{pm} is the reluctance of the PM; R_g is the main air-gap reluctance; R_{ag} is the axis air-gap reluctance; R_{st} is the stator core reluctance; R_{by} is the back yoke reluctance; R_r is the radial rotor reluctance; R_{ar} is the axis rotor reluctance; R_{ab} and R_{ab1} are the axis magnetic bridge; R_{rb} and R_{rb1} are the radial magnetic bridge; $R(i_d, i_q)$ is the rotor magnetic bridge reluctance; $R_s(i_d, i_q)$ is the rotor magnetic barrier reluctance.

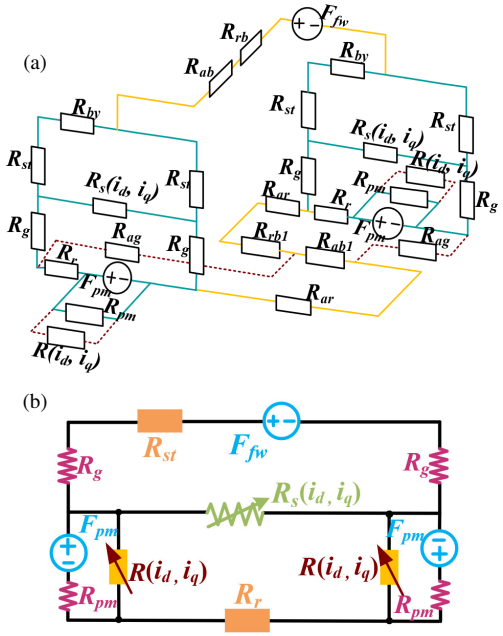

FIGURE 3. Equivalent magnetic circuit model. (a) Three-dimensional equivalent magnetic circuit. (b) Simplified model of (a).

Neglecting the axial magnetic resistance of the solid iron core, the three-dimensional equivalent magnetic circuit can be simplified to the two-dimensional equivalent magnetic circuit as shown in Fig. 3(b). From Fig. 3(b), the main air-gap flux Φ_δ can be obtained as below:

$$\Phi_\delta = \frac{F_i + 2\xi F_{pm}}{2R_g + R_{st} + R_r + 2\xi R_{pm}} \tag{14}$$

$$\xi = \frac{R(i_d, i_q)}{R_{pm} + R(i_d, i_q)} \tag{15}$$

To simplify the analysis, magnetic saturation is not considered in the equivalent magnetic circuit model. Based on the operating principle of the proposed HE-VLFM, the calculation of the main air-gap flux can be derived from Eq. (5). This shows that the main air-gap flux is determined by the MMF generated by PM and FW, respectively. The total flux of the PM is divided into two parts. One part is connected to the turns of the armature windings and is called main PM flux. The other part passes through the rotor magnetic bridge reluctance and is called PM leakage flux. The flux generated by the armature MMF also passes through the rotor magnetic bridge. The rotor bridge reluctance changes when different magnitudes and directions of current are passed. When I_f is a flux-enhancing current, F_i and F_{pm} are in the same direction, and when I_f is flux-weakening current, F_i and F_{pm} are in opposite directions. To change the magnitude and direction of the field winding F_i can alter the magnitude of the main air-gap flux, realizing the adjustment of the air-gap field.

4. ELECTROMAGNETIC PERFORMANCE

HE-VLFM is evaluated using 3D finite element analysis. The excitation magnetic path of HE-VLFM is axially three-dimensional, and its performance cannot be modeled using 2D finite element analysis. In addition, the two-dimensional finite element simulation analysis ignores the axial flux leakage and end effect, which cannot reflect the real situation of the machine well. The no-load air gap flux density, magnetic field distribution, no-load back-EMF, torque characteristics, and flux regulation capability of the investigated machine are analyzed.

4.1. 3D of Air-Gap Flux Density

In order to accurately observe the variation of the no-load air gap flux density of the HE-VLFM at different field winding currents, the magnetostatic field analysis of the HE-VLFM is performed, as shown in Fig. 4. The no-load air-gap flux densities of HE-VLFM in the flux-weakening and flux-enhancing states are shown in Figs. 4(a) and (b), in which the magnitude of the no load air gap flux density is 0.34 T for the flux-weakening state (FW MMF $= -375$ AT) and 0.45 T for the flux-enhancing state (FW MMF $= 375$ AT). The magnitude of HE-VLFM varies by 24.4% in the flux-enhancing and flux-weakening states. Thus, the axial field winding MMF has a superior flux regulation effect on the main air-gap field.

4.2. Flux Density Distribution

The 3D magnetic field distribution of the rotor and magnetic bridge structure of the proposed HE-VLFM at different field winding MMFs are plotted in Fig. 5. The field winding MMF has a great influence on the magnetic field regulation effect of the main magnetic circuit and the saturation depth of the axial magnetic circuit. When the FW MMF is -375 AT, there is local saturation in the axial magnetic circuit. The magnetic density of

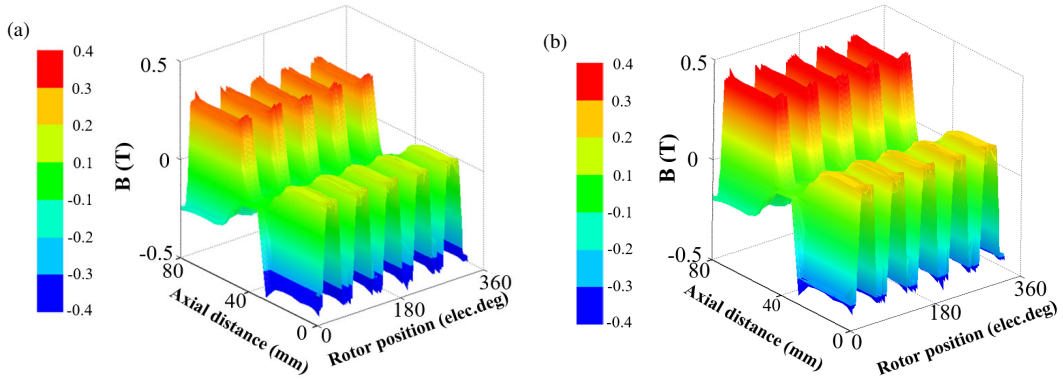

FIGURE 4. Air gap flux density under different field winding MMF. (a) Field winding MMF −375 AT. (b) Field winding MMF 375 AT.

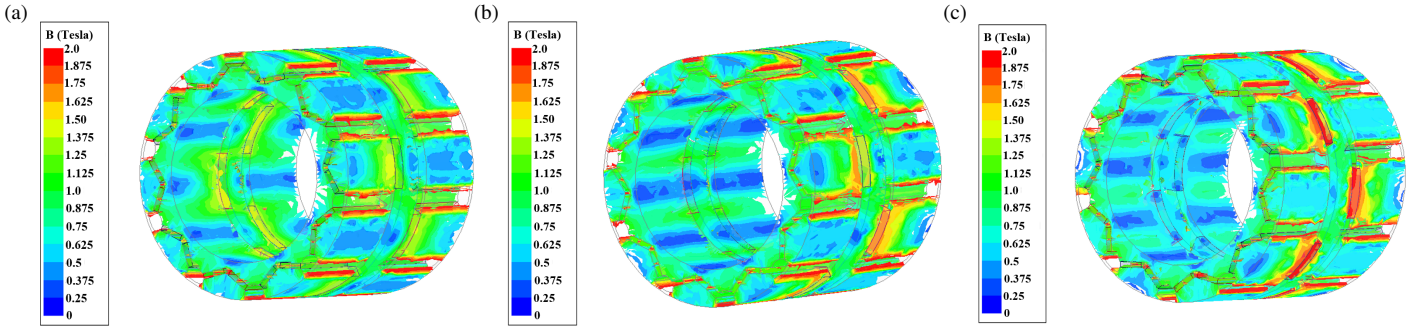

FIGURE 5. Flux density distribution of the rotor and magnetic bridge structure. (a) Field winding MMF −375 AT in HE-VLFM. (b) No-load state in HE-VLFM. (c) Field winding MMF 375 AT in HE-VLFM.

the outer magnetic bridge is 1.25 T, as shown in Fig. 5(a). As the FW current I_f gradually increases, the local saturation of the axial magnetic circuit continues to increase. When FW current I_f is 0, the magnetic density of the outer magnetic bridge is 1.55 T, as shown in Fig. 5(b). As the FW current I_f gradually increases, the local saturation of the axial magnetic circuit continues to increase. However, the extent of saturation of the inner magnetic bridge decreases compared to Fig. 5(a), at which time the flux density of the inner magnetic bridge is 1.2 T. It is because the increase of FW current I_f counteracts the axial component of the PM MMF. When the field winding magnetomotive force is 375 AT, the axial magnetic circuit is reversed, which will further enhance the magnetic field of the main magnetic circuit, and the extent of saturation of the axial magnetic circuit is further increased. The magnetic density of the outer magnetic bridge is 1.88 T, and the magnetic density of the inner magnetic bridge is 0.76 T. At this time, the FW magnetic field basically counteracts the axial component of the PM magnetic field, and the extent of axial magnetic circuit saturation is the lowest.

4.3. Open-Circuit Condition

The characteristics of the machine under field winding MMF is examined through the waveform and spectral analysis of the no-load flux linkage under different FW MMFs, as presented in Fig. 6. The flux linkages are negative at all rotor position electrical angles of 0° and zero at all rotor electrical position angles

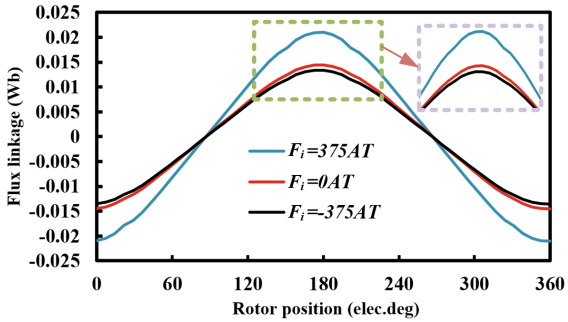

FIGURE 6. No-load flux linkage waveforms under different field winding MMF.

of 90° and 270°. The variation of the amplitude of the flux linkage verifies the process of flux-enhancing and flux-weakening. It is noteworthy that in the case of flux-enhancing the flux linkage amplitude for FW MMF of 375 AT is 0.021 Wb, which is a 42.8% increase in the flux linkage amplitude compared to the flux linkage amplitude for FW MMF of 0 AT with only PM excitation. The condition of maximum flux linkage is realized. It is clear that the flux generated by the DC excitation can be superimposed on the main flux generated by the PM machine, which leads to a change in the flux linkage.

Figure 7 gives the no-load back-EMF of the HE-VLFM under different FW MMFs. F_i = 375 AT, 0 AT, and −375 AT represent the flux-weakening condition with −375 AT, only PM excitation, and flux-enhancing condition with 375 AT, respec-

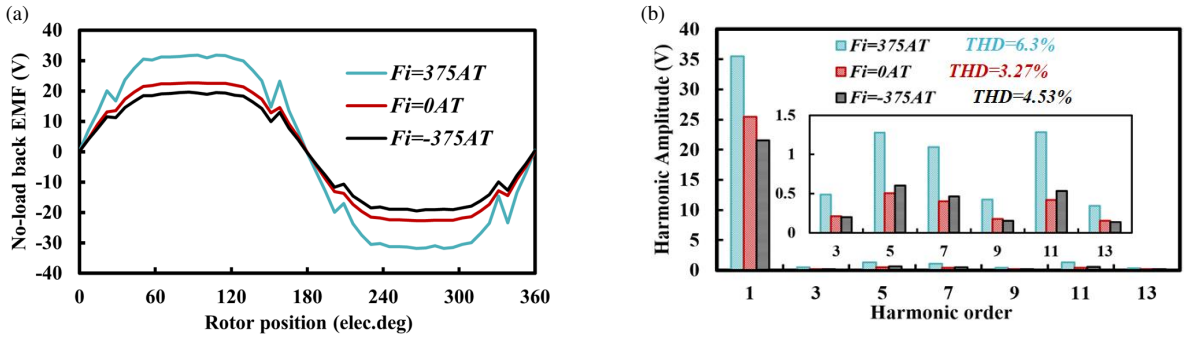

FIGURE 7. Open-circuit back-EMF waveforms and harmonic under different FW MMF. (a) Waveforms. (b) Harmonic.

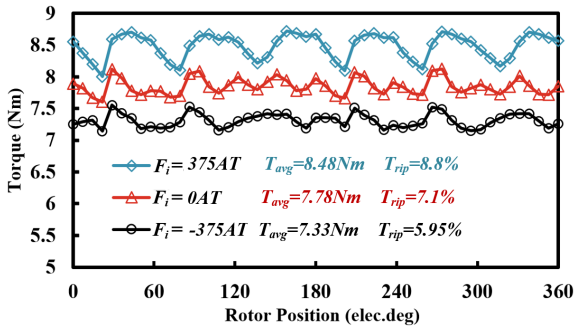

FIGURE 8. Average torque at the armature current density of 5 A/mm^2 under different FW MMF.

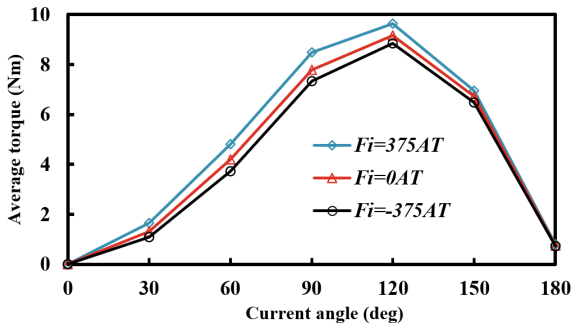

FIGURE 9. Average torque against current angle at the armature current density of 5 A/mm^2 with different FW MMF.

tively. The no-load back-EMF amplitude of HE-VLFM without FW MMF is 25.48 V, subject to axial flux-enhancing and flux-weakening (FW MMF $=\pm 375$ AT). The amplitude of no-load back-EMF in flux-weakening is 21.59 V and in flux-enhancing is 35.49 V, as shown in Fig. 7(a). The amplitude of the no-load EMF of HV-VLFM varies by 39.16% in the flux-enhancing and flux-weakening states so that the HE-VLFM has a better regulation of the main magnetic field by the axis FW MMF. No-load back-EMF waveform is one of the factors affecting torque ripple, so a sinusoidal no-load back-EMF waveform can reduce torque ripple to a certain extent. Then, the back-EMF waveform is analyzed through the Fast Fourier Transform (FFT) as shown in Fig. 7(b). In order to reduce the sinusoidal distortion rate of the voltage waveform, the pole-arc coefficient of HE-VLFM is optimized. To further quantify the FW MMF harmonics, the sinusoidal distortion rate of the FW MMF was calculated according to Eq. (6).

$$\mathrm{THD} = \frac{\sqrt{U_2^2 + U_3^2 + \cdots + U_\nu^2}}{U_1} \times 100\% \qquad (16)$$

where U_ν is the RMS value of the νth order in line voltage, and U_1 is the RMS value of fundamental in line voltage.

It can be seen that the harmonic distortions of FW MMF for 375 AT, 0 AT, and -375 AT are 6.3%, 3.27%, and 4.53%, respectively. The nonuniform air gap created by the magnetic barrier enables the HE-VLFM to have a well-characteristic sinusoidal no-load back-EMF, although the harmonics generated by the fractional-slot centralized windings on the stator affect the back-EMF to some extent.

4.4. Torque Characteristics

Figure 8 shows the comparative waveforms of torque and torque ripple at the armature current density of 5 A/mm^2 under different FW MMF excitations. The average torque at only PM excitation in the flux-weakening state and flux-enhancing state are 8.48 Nm, 7.78 Nm, and 7.33 Nm, respectively, and the torque ripples are 8.8%, 7.1% and 5.95%, respectively. Compared with the output torque of FW MMF of AT, the output torque of FW MMF of $+375$ AT is increased by 17.8%. The output torque capability of the machine is effectively improved in the flux-enhancing state.

The waveform plots of average torque versus current angle at the armature current density of 5 A/mm^2 for different FW MMF excitations are shown in Fig. 9. The maximum torque is 9.64 Nm for an FW MMF of $+375$ AT, which is a 4.8% increase in the maximum torque compared to the case where the FW MMF is 0 AT. Therefore, it is more effective in the flux-enhancing condition (positive FW excitation) because the negative i_d current tends to alleviate the flux saturation.

The average torque against current angle FW and AC excitation currents are illustrated in Fig. 10. When the current angle is 30°, the average torque reaches the maximum, and the average torque increases with the increase of the excitation current. Taking 30° current angle as an example, i_q is 4.66 A at this time; the average torque is 10.5 Nm when the excitation current is -15 A; and the average torque is 11.17 Nm when the FW current is 15 A, which is a 5.9% change in torque. This shows that the FW excitation current can effectively regulate the electromagnetic torque. According to the back-EMF regu-

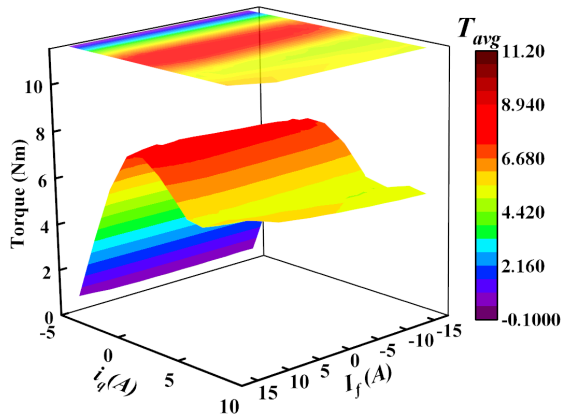

FIGURE 10. Average torque against current angle under FW and AC excitation currents.

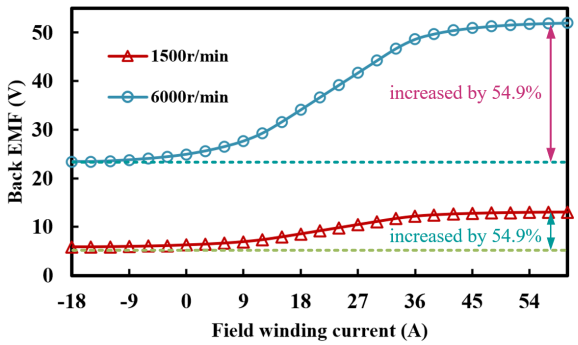

FIGURE 11. No-load flux regulation characteristic of HE-VLFM.

lation, magnetic saturation does not flux-enhancing as much as magnetic saturation flux-weakening.

4.5. Flux Regulation Capability

For hybrid excitation machines, the flux regulation capability is a critical indicator of the electromagnetic performance of the machine. The flux regulation capability indicates the influence of the field winding flux on the main flux, which can be defined as:

$$\sigma = \frac{E_e - E_w}{E_{pm}} \tag{17}$$

where E_e is the maximum value of the back-EMF in the flux-enhancing condition, E_w the maximum value of the back-EMF in the flux-weakening condition, and E_{pm} the maximum value of the back-EMF generated by PM excitation rather than FW field winding. It is worth noting that the ratio of flux regulation is defined in the no-load state. As shown in Fig. 7(a), the maximum values of the no-load back-EMF in the flux-weakening state, flux-enhancing state, and only PM excitation state are 8.88 V, 9.57 V, and 14.02 V, respectively. Calculated from Eq. (6), the ratio of the flux regulating capability of the HE-VLFM is 50.1%, which indicates that the machine has a superior flux regulating capability.

Figure 11 reflects the relationship between the rms value of the no-load back-EMF and the field winding current of the HE-VLFM at different speeds. When the excitation current is increased from -18 A to 54 A, the rms of no-load back-EMF increases by 54.9%, which reflects that HE-VLFM has good flux regulating characteristics from the other side. When the excitation current is less than zero, the rms value of no-load back-EMF is basically unchanged. But when the excitation current is greater than zero, the rms value of no-load back-EMF increases with the increase of excitation current. When the excitation current increases to a certain value, the machine tends to be saturated, and the effective value of no-load back-EMF no longer increases. The flux regulation ability is basically the same at 1500 r/min and 6000 r/min.

4.6. Overload Capacity

The electromagnetic average torque versus excitation current density for HE-VLFM is plotted in Fig. 12. The excitation current density of 6 A/mm^2 is noted as the rated excitation current density, which corresponds to the torque of 8.94 Nm. When HE-VLFM is in climbing or heavy load conditions, the current needs to be increased. The reasonable design of the rotor magnetic barrier makes the iron core less likely to be saturated. When the FW MMF is $+375$ AT, and the excitation current density is 6 A/mm^2, the average torque is 9.47 Nm, which increases by 5.5% compared with the FW MMF of 0 AT. When the field winding density increases to 12 A/mm^2, its average torque is 12.83 Nm, which is 1.35 times of the field winding of 6 A/mm^2. HE-VLFM is characterized by good overload capability.

4.7. Generator Mode Load Characteristic

According to the principle of electromechanical energy conversion, any permanent magnet synchronous motor has the capability to function as a permanent magnet synchronous generator. However, due to distinct performance requirements in both operating states of generators and machines, their magnetic circuit structure, parameter analysis, and electromagnetic performance calculation exhibit similarities as well as unique characteristics.

In order to verify the output voltage constancy capability of HE-VLFM operating as a generator mode, the variation curves of phase voltage with load current at different excitation currents, i.e., the load characteristic curves of the generator, are analyzed at 5500 r/min as shown in Fig. 13. It can be seen that the terminal voltage decreases with increasing load current at 5500 r/min. When the load current is the same, the end voltage increases with the increase of excitation current. When FW MMF is $+375$ AT, the regulation range of the end voltage is 24.7%. When FW MMF is 0 AT, the regulation range of the end voltage is 25.73%. When FW MMF is -375 AT, the adjustment range of the end voltage is 26.5%. The regulation range is slightly smaller because the permanent magnet is the main excitation source in generator mode.

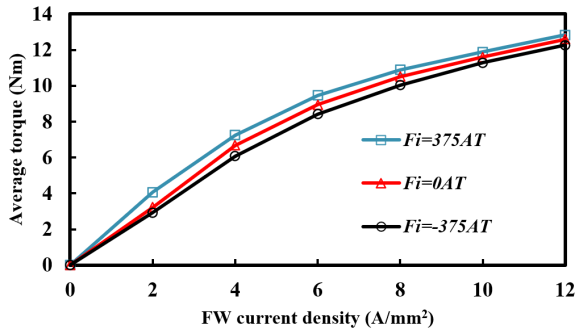

FIGURE 12. Electromagnetic average torque versus field winding current density of HE-VLFM.

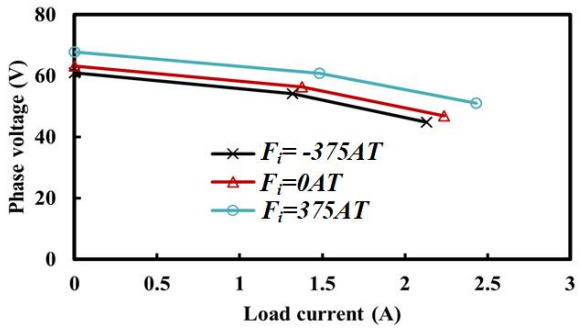

FIGURE 13. Phase voltage as a function of load current at 5500 r/min.

TABLE 2. Comparison results of the HE-VLFM.

	+375 AT	0 AT	−375 AT
Average torque (Nm)	8.84	7.78	7.33
Torque ripple (%)	8.8	7.1	5.95
Air-gap density (T)	0.46	/	0.38
EMF Amplitude (V)	35.49	25.48	21.58
Flux linkage (Wb)	0.021	0.014	0.012
Peak torque (Nm)	9.64	9.2	8.9
Efficiency (%)	95%	90%	92%
Voltage regulation (%)	24.7%	25.73%	26.5%

5. CONCLUSION

A hybrid excitation variable-leakage-flux machine (HE-VLFM) for electric vehicles is presented in this paper. The machine mainly consists of stator, rotor, magnetic bridge, field winding, and armature winding. The rational design between the magnetic bridge and rotor enables the machine to generate an axial magnetic circuit, which regulates the air gap flux by altering the field winding current. Additionally, the comparison results of the HE-VLFM are examined. Firstly, Table 2 presents the average torque, torque ripple, no-load air-gap density, no-load back-EMF amplitude, flux linkage, efficiency, and voltage regulation. It is evident that the proposed HE-VLFM demonstrates superior output torque capability primarily at +375 AT level. As a result, this leads to a significantly expanded speed range for the proposed machine. The following conclusions were drawn.

(1) The HE-VLFM proposed in this paper combines the advantages of hybrid excitation characteristics and variable leakage flux characteristics to enhance the air gap regulation range through dual characteristics.

(2) With increasing excitation current up to magnetic saturation, the air gap adjustment range of HE-VLFM can go up to 54.9%.

(3) HE-VLFM has improved the electromagnetic torque by 19.8% and the no-load back-EMF by 35.77% in the magnetized state. From the flux-weakening state to the flux-enhancing state, the no-load back-EMF changes by 50.1%.

(4) Under overload conditions, the HE-VLFM achieves 1.35 times of the rated torque output.

ACKNOWLEDGEMENT

This work at Jiangxi University of science and technology was sponsored by the National Natural Science Foundation of China (NNSFC) under Grant No. 52067008, Jiangxi University of Science and Technology High-level Talents Research Special Funds 205200100710.

REFERENCES

[1] Wang, C., Z. Zhang, and J. Han, "Multiobjective optimization of high power density outer rotor PM starter generator considering electromagnetic and temperature characteristics," *IEEE Transactions on Industrial Electronics*, Vol. 71, No. 8, 8339–8350, Aug. 2024.

[2] Xiao, Y., Z. Q. Zhu, G. W. Jewell, J. T. Chen, D. Wu, and L. M. Gong, "A novel asymmetric interior permanent magnet synchronous machine," *IEEE Transactions on Industry Applications*, Vol. 58, No. 3, 3370–3382, May-Jun. 2022.

[3] Tapia, J. A., F. Leonardi, and T. A. Lipo, "Consequent-pole permanent-magnet machine with extended field-weakening capability," *IEEE Transactions on Industry Applications*, Vol. 39, No. 6, 1704–1709, 2003.

[4] Yang, H., S. Lyu, H. Lin, Z. Zhu, H. Zheng, and T. Wang, "A novel hybrid-magnetic-circuit variable flux memory machine," *IEEE Transactions on Industrial Electronics*, Vol. 67, No. 7, 5258–5268, Jul. 2020.

[5] Yang, H., Z. Q. Zhu, H. Lin, P. L. Xu, H. L. Zhan, S. Fang, and Y. Huang, "Design synthesis of switched flux hybrid-permanent magnet memory machines," *IEEE Transactions on Energy Conversion*, Vol. 32, No. 1, 65–79, Mar. 2017.

[6] Fan, W., X. Zhu, L. Quan, W. Wu, L. Xu, and Y. Liu, "Flux-weakening capability enhancement design and optimization of a controllable leakage flux multilayer barrier PM motor," *IEEE Transactions on Industrial Electronics*, Vol. 68, No. 9, 7814–7825, Sep. 2021.

[7] Zhang, L., S. Han, X. Zhu, L. Quan, and W.-H. Chen, "Research on five-phase flux-intensifying permanent magnet motor drive system based on new active sensorless strategy," *IEEE Transactions on Transportation Electrification*, Vol. 9, No. 3, 4266–4277, Sep. 2023.

[8] Yang, H., H. Lin, and Z. Q. Zhu, "Recent advances in variable flux memory machines for traction applications: A review," *CES Transactions on Electrical Machines and Systems*, Vol. 2, No. 1, 34–50, Mar. 2018.

[9] Zhu, X., D. Fan, L. Mo, Y. Chen, and L. Quan, "Multiobjective optimization design of a double-rotor flux-switching perma-

nent magnet machine considering multimode operation," *IEEE Transactions on Industrial Electronics*, Vol. 66, No. 1, 641–653, Jan. 2019.

[10] Limsuwan, N., T. Kato, K. Akatsu, and R. D. Lorenz, "Design and evaluation of a variable-flux flux-intensifying interior permanent-magnet machine," *IEEE Transactions on Industry Applications*, Vol. 50, No. 2, 1015–1024, Mar.-Apr. 2014.

[11] Fukushige, T., N. Limsuwan, T. Kato, K. Akatsu, and R. D. Lorenz, "Efficiency contours and loss minimization over a driving cycle of a variable flux-intensifying machine," *IEEE Transactions on Industry Applications*, Vol. 51, No. 4, 2984–2989, Jul.-Aug. 2015.

[12] Xu, L., X. Zhu, W. Wu, W. Fan, X. Zhou, X. Cai, and L. Quan, "Flux-leakage design principle and multiple-operating conditions modeling of flux leakage controllable pm machine considering driving cycles," *IEEE Transactions on Industrial Electronics*, Vol. 69, No. 9, 8862–8874, Sep. 2022.

[13] Yang, H., Y. Li, Y. Huang, R. Tu, D. Liu, H. Lin, and Z. Q. Zhu, "A novel variable-leakage-flux interior permanent magnet machine with segmented trapezoidal magnet configuration," in *2023 IEEE Energy Conversion Congress and Exposition (ECCE)*, 4228–4235, Nashville, TN, USA, 2023.

[14] Li, J., K. Wang, S. S. Zhu, and C. Liu, "Integrated-induction-based hybrid excitation brushless DC generator with consequent-pole rotor," *IEEE Transactions on Transportation Electrification*, Vol. 8, No. 2, 2233–2248, Jun. 2022.

[15] Ayub, M., G. Jawad, and B.-I. Kwon, "Consequent-pole hybrid excitation brushless wound field synchronous machine with fractional slot concentrated winding," *IEEE Transactions on Magnetics*, Vol. 55, No. 7, 1–5, Jul. 2019.

[16] Shen, Y. and Q. Lu, "Design and analysis of hybrid-excited flux modulated linear machines with zero-sequence current excitation," *IEEE Journal of Emerging and Selected Topics in Power Electronics*, Vol. 10, No. 2, 1834–1846, Apr. 2022.

[17] Zhao, X., S. Niu, X. Zhang, and W. Fu, "A new relieving-DC-saturation hybrid excitation vernier machine for HEV starter generator application," *IEEE Transactions on Industrial Electronics*, Vol. 67, No. 8, 6342–6353, Aug. 2020.

[18] Farahzadi, M., K. Abbaszadeh, and S. Mirnikjoo, "Electromagnetic-thermal analysis of a hybrid-excited flux switching permanent magnet generator for wind turbine application," *IEEE Transactions on Energy Conversion*, Vol. 38, No. 3, 1962–1973, Sep. 2023.

[19] Cai, S., Z. Q. Zhu, J.-C. Mipo, and S. Personnaz, "A novel parallel hybrid excited machine with enhanced flux regulation capability," *IEEE Transactions on Energy Conversion*, Vol. 34, No. 4, 1938–1949, Dec. 2019.

[20] Fodorean, D., A. Djerdir, I.-A. Viorel, and A. Miraoui, "A double excited synchronous machine for direct drive application — Design and prototype tests," *IEEE Transactions on Energy Conversion*, Vol. 22, No. 3, 656–665, Sep. 2007.

[21] Kamiev, K., J. Nerg, J. Pyrhönen, V. Zaboin, V. Hrabovcová, and P. Rafajdus, "Hybrid excitation synchronous generators for island operation," *IET Electric Power Applications*, Vol. 6, No. 1, 1–11, 2012.

[22] Liu, Y., Z. Zhang, and X. Zhang, "Design and optimization of hybrid excitation synchronous machines with magnetic shunting rotor for electric vehicle traction applications," *IEEE Transactions on Industry Applications*, Vol. 53, No. 6, 5252–5261, Nov.-Dec. 2017.

[23] Sun, L., Z. Zhang, L. Yu, and X. Gu, "Development and analysis of a new hybrid excitation brushless DC generator with flux modulation effect," *IEEE Transactions on Industrial Electronics*, Vol. 66, No. 6, 4189–4198, Jun. 2019.

[24] Cai, S., Z. Q. Zhu, S. Mallampalli, J.-C. Mipo, and S. Personnaz, "Investigation of novel fractional slot nonoverlapping winding hybrid excited machines with different rotor topologies," *IEEE Transactions on Industry Applications*, Vol. 57, No. 1, 468–480, Jan.-Feb. 2021.